2013 IEEE/RSJ International Conference on
Intelligent Robots and Systems (IROS)
November 3-7, 2013. Tokyo, Japan

Adaptive Control for Takeoff, Hovering, and Landing of a Robotic Fly

Pakpong Chirarattananon, Kevin Y Ma, and Robert J Wood

Abstract— **Challenges for controlled flight of a robotic insect are due to the inherent instability of the system, complex fluid-structure interactions, and the general lack of a complete system model. In this paper, we propose theoretical models of the system based on the limited information available from previous work and a comprehensive adaptive flight controller that is capable of coping with uncertainties in the system. We have demonstrated that the proposed methods enable the robot to achieve sustained hovering flights with relatively small errors compared to a similar but non-adaptive approach. Furthermore, vertical takeoff and landing flights are also shown to illustrate the fidelity of the flight controller.**

I. Introduction

Inspired by the agility of flying insects and motivated by the myriad engineering challenges and open scientific questions, the RoboBees projects is developing a colony of autonomous robotic insects. In [1], controlled flight of a millimeter-scale flapping-wing robot was first empirically demonstrated. This result was the culmination of research in meso-scale actuation [2] and advances in manufacturing [3]. These developments enabled the creation of insect-scale flapping-wing vehicles that are able to generate torques about all three body axes [4], [5]; a requirement for flapping-wing MAVs due to their inherent instability [6].

Primary challenges encountered in the task of controlling the robotic insect shown in Fig. 1 are due to the lack of comprehensive knowledge of the system and the variation in system properties owing to complex aerodynamics and manufacturing imperfections. Empirical characterization and system identification are not currently feasible since a multi-axis force/torque sensor with appropriate range and resolution for the robots of interest does not exist. To compensate, in previous work [1], predictions of system's characteristics were made based on theoretical models [7], [8]. In order to achieve sustained flight, it is necessary to account for uncertain parameters arising from manufacturing errors (e.g. torque offsets); this cannot be done by modeling alone. One possible approach to account for model uncertainties is to use an adaptive controller.

This work was partially supported by the National Science Foundation (award number CCF-0926148), and the Wyss Institute for Biologically Inspired Engineering. Any opinions, findings, and conclusions or recommendations expressed in this material are those of the authors and do not necessarily reflect the views of the National Science Foundation.

The authors are with the School of Engineering and Applied Sciences, Harvard University, Cambridge, MA 02138, USA, and the Wyss institute for Biologically Inspired Engineering, Harvard University, Boston, MA, 02115, USA (email: chirarat@fas.harvard.edu; kevinma@seas.harvard.edu; rjwood@eecs.harvard.edu).

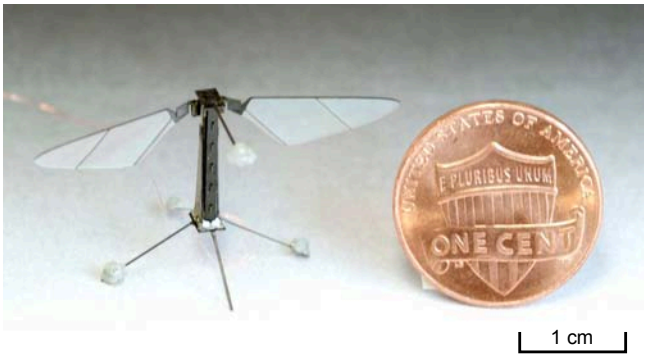

Fig. 1. Photograph of a flapping-wing microrobot prototype alongside a US penny. The robot, equipped with two bimorph piezoelectric actuators, weighs 80mg including four retroreflective markers for use in flight control experiments.

The controllers used in [1] were not inherently adaptive. Instead, an integral part was added to deal with parameter uncertainty. It is conceivable that the use of adaptive controllers with proven convergence properties could potentially improve flight performance. Additionally, the results allow us to gain further insights into the flight dynamics of the vehicle and obtain more realistic models for control purposes. In this paper we revisit the problem of controlling the robotic insect by employing an adaptive approach. The flight controller has been designed based on proposed Lyapunov functions. The control laws and adaptive laws are derived such that the stability can be guaranteed in a Lyapunov sense. The major benefit of the approach is the reliability of the adaptive parts that allow us to efficiently obtain estimates of uncertain parameters. The performance of the proposed controller is verified in hovering flights and vertical takeoff and landing flights.

The rest of the paper is organized as follows. Section II briefly covers the description of the microrobot used in the experiment and its relevant flight dynamics. The details on its thrust and torque generation, including coupling are explained in Section III. The derivations of the controllers are given in Section IV. Section V contains the implementation and flight experiments. Finally, further considerations and future work are discussed in Section VI.

II. Robot Description and Flight Dynamics

A. Robot description

The robot in this study (illustrated in Fig. 1) is an 80mg flapping-wing microrobot fabricated using the *Smart Composite Microstructures* (SCM) process as detailed in [4],

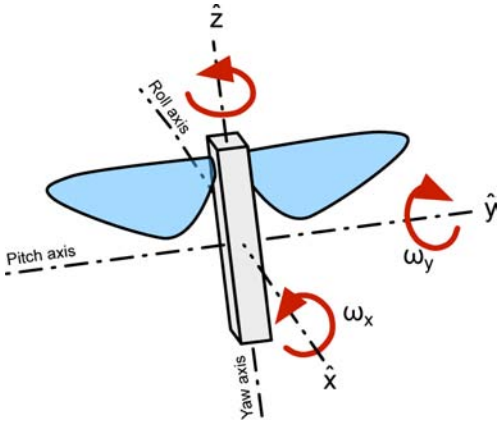

Fig. 2. Definitions of the body frame and roll, pitch, and yaw axes.

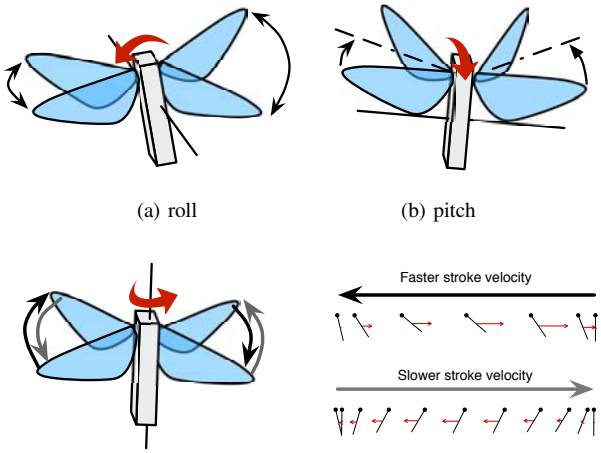

Fig. 3. Different flapping schemes for body toque generation. (a) Roll torque is generated by introducing differential stroke amplitude between the two wings. (b) Pitch torque is produced by shifting the mean stroke angle of both wings forwards or backwards. (c) Yaw torque is obtained by having a difference in stroke velocity between the upstroke and the downstroke, the black and grey arrows correspond to arrows in (d). (d) The effect of stroke velocity on a wing's drag force. The imbalance in instantaneous drag results in a net drag force per wing stroke cycle, and hence yaw torque.

[1]. The robot is equipped with two piezoelectric bimorph actuators such that each wing can be driven independently. Linear displacement of the actuator tip is amplified and converted into a rotational motion of the wing by a flexure-based transmission, creating an actuator-transmission-wing system. In operation, the flapping frequency is typically fixed at a value between $110 - 120$Hz, near the system's resonant frequency. The robotic insect is capable of modulating the thrust force that is nominally aligned with the robot's vertical axis by altering its flapping amplitude and able to generate torques along its three body axes using different flapping schemes as shown in [4], [1]. Theoretically, this allows the robot to be controllable over the $SO(3)$ space. Consequently, lateral maneuvers can be achieved by reorienting the body such that the net thrust vector takes on a lateral component.

B. Flight Dynamics

Owing to the relatively small inertia of the wings (relative to the body) and rapid but low-amplitude motion of the actuators, for the time scales of interest, these small oscillations can be neglected. The robotic insect is then regarded as a rigid body in three-dimensional space. In the body attached coordinates, the roll, pitch, and yaw axes are aligned with the $\hat{x}$, $\hat{y}$, and $\hat{z}$ axes as presented in Fig. 2.

Due to symmetry, it is reasonable to assume that the cross terms in the moment of inertia matrix $\mathbf{J}$ are negligible. The orientation between the body frame and the inertial frame is defined by the rotation matrix R, which is rotating at an angular velocity ω with respect to the body frame. As a result, the attitude dynamics can be described by the Euler equation

$$\mathbf{J}\dot{\omega} \quad = \quad \sum \tau - (\omega \times \mathbf{J}\omega)\,, \tag{1}$$

where $\Sigma\tau_i$ is the total torque acting on the vehicle. The relation between the rotation matrix and the angular velocity is given as

$$\begin{bmatrix} \omega_x \\ \omega_y \\ \omega_z \end{bmatrix} = \begin{bmatrix} R_{13}\dot{R}_{12} + R_{23}\dot{R}_{22} + R_{33}\dot{R}_{32} \\ R_{11}\dot{R}_{13} + R_{21}\dot{R}_{23} + R_{31}\dot{R}_{33} \\ R_{12}\dot{R}_{11} + R_{22}\dot{R}_{21} + R_{32}\dot{R}_{31} \end{bmatrix}. \tag{2}$$

The lateral dynamics of the robot near hovering, when the robot is generating thrust equal to its own weight, can be simplified to a two-dimensional second-order system. Assuming the vehicle is only slightly deviated from a vertical orientation, the lateral force generated by the robot is approximately proportional to the deviation of the robot's $\hat{z}$ axis from the vertical. Therefore, lateral forces in the dynamics can be expressed in terms of the rotation matrix as

$$m\frac{d^2}{dt^2}\begin{bmatrix} X \\ Y \end{bmatrix} = F_z \begin{bmatrix} R_{13} \\ R_{23} \end{bmatrix} = mg \begin{bmatrix} R_{13} \\ R_{23} \end{bmatrix}, \tag{3}$$

where m denotes the mass of the robot, g is the gravitational constant, and X, Y are lateral position in the inertial frame. Here we have ignored aerodynamic damping, which is predominantly caused by the flapping wings. The damping, however, should be insignificant while the robot is stationary during hovering.

III. Thrust and Torque Generation

In [4], it was shown that the thrust produced by the robotic insect is approximately a linear function of the actuator voltage. The robot was capable of producing thrust larger than 1.3mN, or more than 1.5 times its own weight. Body torques on the order of one μNm can be achieved by using the three different flapping schemes illustrated in Fig. 3.

The key challenge in obtaining a map or a transfer function between input signals and the resultant thrust or torques is the lack of viable multi-axis force/torque sensor. In [4], a custom dual-axis force-torque capacitive sensor similar to the design in [9] was used to measure a single axis of torque and a single force perpendicular to the torque axis. This sensor, therefore,

cannot determine the coupling between torques along different axes. Furthermore, despite over a decade of progress in micromanufacturing, there still exists considerable variation between robots. In addition, the process of mounting the robot on the sensor is challenging and possibly destructive, making it impractical to characterize all robots prior to the flight experiments.

As a consequence, a more theoretical approach is taken. Based on a model of flapping wings with passive rotation [7], we constructed a theoretical approximation of time-averaged thrust and torques as a function of wing trajectory. A linearized model of the actuator-transmission-wing system (from [8]) is then employed to estimate the required drive signals to obtain the desired wing trajectory. These steps are explained in more detail below.

A. Wing trajectory for thrust and torque generation

In [7], the blade-element method was used to provide aerodynamic force and moment estimates to predicted wing rotational dynamics. Herein, this model is used to compute the estimates of the resultant thrust and body torques using the flapping schemes shown in Fig. 3. The model confirms minimal coupling between three torque generation modes, and a linearized map can be expressed as the following:

$$\begin{aligned} F_t &= \alpha_t \Phi - \beta_t \\ \tau_r &= (\alpha_r \Phi - \beta_r)\,\Theta_r \\ \tau_p &= (\alpha_p \Phi - \beta_p)\,\Theta_p \\ \tau_y &= (\alpha_y \Phi - \beta_y)\,\eta, \end{aligned} \tag{4}$$

where F_t denotes the thrust, τ_i's represent roll, pitch, and yaw torques, Φ is the flapping amplitude, Θ_r is a differential stroke angle, Θ_p is the shift in mean stroke angle, η is a relative proportion of a second-harmonic signal used for generating imbalanced drag forces, and the α_i and β_i terms are resulting constants from the linearization. Equation (4) suggests thrust is only dependent on the mean flapping amplitude (for a fixed frequency) and body torques are proportional to their respective input parameters. This is supported by the experimental results described in Section V.

B. Actuator-transmission-wing system dynamics

Once we have obtained the required wing trajectory for the desired thrust and torques from equation (4), the corresponding actuator drive signals are calculated according to the simplified second order linear model of the actuator-transmission-wing dynamics [8]. For example, a shift in the mean stroke angle translates to a DC offset in the drive signal. The model enables us to calculate the voltage amplitudes and offsets required to generate thrust to stay aloft and torques for control. Based on the predictions, one could then ensure that the total voltage required does not exceed the maximum actuator voltage.

IV. Flight Controller

Driven by the lack of both empirical measurements and an accurately identified model of the robot as stated in section III, we employed an adaptive controller in order to estimate unknown parameters. The overall flight controller is comprised of three subcontrollers: lateral controller, attitude controller, and altitude controller. The lateral controller takes position feedback from a motion capture system and determines the desired orientation of the robot in order to maneuver the robot to a position setpoint. This desired orientation serves as the setpoint for the attitude controller that evaluates the required torques from the vehicle to achieve the desired attitude. In parallel, the altitude controller computes the suitable thrust force to maintain the robot at the desired height based on the position feedback. These controllers are considerably different from those in [1] as they employ the use of sliding mode control techniques [10] for adaptive purposes. Moreover, higher order model of lateral and altitude dynamics are implemented to reduce the oscillating behaviors seen in the results from [1].

A. Adaptive Attitude Controller

A consensus drawn from several stability studies indicates that, similar to insect flight, flapping-wing MAVs in hover are unstable without active control [6]. Together with uncertainties due to an incomplete model of the vehicle and the requirement to vary the attitude setpoint for lateral maneuvers, it is necessary to design a robust controller that allows for significant excursions from the hovering state. As opposed to traditional linear controllers based on a linearization about hover, we employ Lyapunov's direct method to design a controller with a large domain of attraction. The attitude controller employed here is distinct from the one that demonstrated the first successful flights in [1] as it enables better tracking and adaptive ability for uncertain parameter estimates.

The goal of the attitude controller is to align the robot $\hat{z}$ axis with the desired attitude vector $\hat{z}_d$. Such a strategy allows the robot to maneuver in the desired direction while relaxing control over exact yaw orientation. In other words, the robot has no preference to roll or pitch, but a combination of them would be chosen so that the body $\hat{z}$ axis aligns with the desired attitude vector $\hat{z}_d$ with minimum effort.

Based on a sliding control approach [10], we begin by defining a composite variable composed of an angular velocity vector ω and the attitude error $\mathbf{e}$,

$$\mathbf{s}_a = \omega + \Lambda \mathbf{e}, \tag{5}$$

where Λ is a positive diagonal gain matrix. The attitude error $\mathbf{e}$ is selected to correspond to the amount of the deviation of $\hat{z}$ from $\hat{z}_d$,

$$\begin{aligned} \mathbf{e} &= \begin{bmatrix} \hat{y}\cdot\hat{z}_d & -\hat{x}\cdot\hat{z}_d & 0 \end{bmatrix}^T \\ &= \begin{bmatrix} R_{12} & R_{22} & R_{32} \\ -R_{11} & -R_{21} & -R_{31} \\ 0 & 0 & 0 \end{bmatrix} \begin{bmatrix} \hat{z}_{d1} \\ \hat{z}_{d2} \\ \hat{z}_{d3} \end{bmatrix}. \end{aligned} \tag{6}$$

Note that the third element of the attitude error vector is zero, consistent with the decision not to control the exact yaw orientation. The composite variable $\mathbf{s}_a$ is zero when $\hat{z}$ aligns with $\hat{z}_d$ and the robot has no angular velocity. Let $\hat{\mathbf{a}}$ be a vector containing the estimates of unknown parameters and $\tilde{\mathbf{a}}$ be the estimation error defined as $\tilde{\mathbf{a}} = \hat{\mathbf{a}} - \mathbf{a}$, we propose the following Lyapunov function candidate

$$V_a = \frac{1}{2}\mathbf{s}_a^T \mathbf{J} \mathbf{s}_a + \frac{1}{2}\tilde{\mathbf{a}}\Gamma^{-1}\tilde{\mathbf{a}}, \tag{7}$$

here Γ is a positive diagonal adaptive gain matrix. Assuming that the robot also produces some unknown constant torques $-\tau_o$ in addition to the commanded torque τ_c by the controller, equation (1) can be rewritten as

$$\mathbf{J}\dot{\omega} = \tau_c - \tau_o - (\omega \times \mathbf{J}\omega). \tag{8}$$

As a result, from equations (5), (7) and (8), the time derivative of the Lyapunov function is given by

$$\dot{V}_a = \mathbf{s}_a^T \left(\tau_c - \tau_o - (\omega \times \mathbf{J}\omega) + \mathbf{J}\Lambda\dot{\mathbf{e}}\right) + \dot{\tilde{\mathbf{a}}}\Gamma^{-1}\tilde{\mathbf{a}}. \tag{9}$$

Defining $\hat{\mathbf{J}}$ as the estimate of the inertia matrix, we propose the control law

$$\begin{aligned} \tau_c &= -K_a\mathbf{s}_a + \hat{\tau}_o - \left(\Lambda\mathbf{e} \times \hat{\mathbf{J}}\omega\right) - \hat{\mathbf{J}}\Lambda\dot{\mathbf{e}} && (10)\\ &= -K_a\mathbf{s}_a + Y\hat{\mathbf{a}}, && (11) \end{aligned}$$

where K is a positive diagonal gain matrix, $\hat{\tau}_o$ is an estimate of the unknown offset torque τ_o, and the matrix Y and the parameter estimate vector $\hat{\mathbf{a}}$ are

$$\begin{aligned} Y &= \left[\begin{array}{ccc|c} -\Lambda\dot{\mathbf{e}}_1 & \Lambda\dot{\mathbf{e}}_3\omega_y & -\Lambda\dot{\mathbf{e}}_2\omega_z & \\ -\Lambda\dot{\mathbf{e}}_3\omega_x & -\Lambda\dot{\mathbf{e}}_2 & \Lambda\dot{\mathbf{e}}_1\omega_z & I_{3\times 3} \\ \Lambda\dot{\mathbf{e}}_2\omega_x & -\Lambda\dot{\mathbf{e}}_1\omega_y & -\Lambda\dot{\mathbf{e}}_3 & \end{array}\right] \\ \hat{\mathbf{a}} &= \left[\begin{array}{cccccc} \hat{\mathbf{J}}_{xx} & \hat{\mathbf{J}}_{yy} & \hat{\mathbf{J}}_{zz} & \hat{\tau}_{o1} & \hat{\tau}_{o2} & \hat{\tau}_{o3} \end{array}\right]^T. && (12) \end{aligned}$$

Equation (9) then becomes

$$\dot{V}_a = -\mathbf{s}_a^T K_a \mathbf{s}_a + \mathbf{s}_a^T Y\tilde{\mathbf{a}} + \dot{\tilde{\mathbf{a}}}\Gamma^{-1}\tilde{\mathbf{a}}. \tag{13}$$

This suggests the adaptive law

$$\dot{\hat{\mathbf{a}}} = -\Gamma Y^T \mathbf{s}_a, \tag{14}$$

which renders the time derivative of the Lyapunov function to be negative definite,

$$\dot{V}_a = -\mathbf{s}_a^T K_a \mathbf{s}_a \leq 0. \tag{15}$$

According to the invariant set theorem, the system is theoretically almost globally asymptotically stable. That is, the composite variable and the estimation errors converge to zero. The exception occurs when the $\hat{z}$ axis points in the opposite direction to the desired attitude vector. Additionally, notice that no particular representation of rotation is used, hence no care needs to be taken to avoid a singularity or any ambiguity in the choice of representation.

The presented attitude controller has a few benefits over the controller employed in [1]. For instance, it has better tracking ability, and the adaptive part takes into consideration the torque offset errors and uncertainty in the estimate of the inertia and makes the correction based on the feedback.

B. Adaptive Lateral Controller

The lateral controller is designed based on the dynamics described in equation (3). This controller relies on position feedback to compute the desired attitude vector that is used by the attitude controller. An adaptive part is incorporated in order to account for misalignment between the presumed thrust vector and the true orientation of the thrust vector. Moreover, the lateral controller assumes that the response of the attitude controller can be described by a first order differential equation as shown in equation (16)–this consideration was not present in previous work [1].

$$\frac{d}{dt}\begin{bmatrix} R_{13} \\ R_{23} \end{bmatrix} = \gamma\left(\begin{bmatrix} \hat{z}_{d1} \\ \hat{z}_{d2} \end{bmatrix} - \begin{bmatrix} R_{13} \\ R_{23} \end{bmatrix}\right) \tag{16}$$

Here γ^{-1} is an approximate time constant of the closed-loop attitude dynamics. The complete model of the lateral dynamics is obtained by substituting equation (16) into (3).

$$\begin{aligned} \gamma^{-1} m\frac{d^3}{dt^3}\begin{bmatrix} X \\ Y \end{bmatrix} + m\frac{d^2}{dt^2}\begin{bmatrix} X \\ Y \end{bmatrix} = \\ mg\begin{bmatrix} \hat{z}_{d1} \\ \hat{z}_{d2} \end{bmatrix} + f_1\begin{bmatrix} -R_{11} \\ -R_{21} \end{bmatrix} + f_2\begin{bmatrix} -R_{12} \\ -R_{22} \end{bmatrix}, \end{aligned} \tag{17}$$

where we have also added f_1 and f_2 to represent small unknown misalignment of the thrust vector along the body $\hat{x}$ and $\hat{y}$ axes respectively.

Thus, the controller can be designed based on a similar composite variable idea as used for the attitude controller. The composite variable $\mathbf{s}_l$, and the Lyapunov function candidate V_l are defined as

$$\begin{aligned} \mathbf{s}_l &= \left(\frac{d^2}{dt^2} + 2\lambda\frac{d}{dt} + \lambda^2\right)\begin{bmatrix} \tilde{X} \\ \tilde{Y} \end{bmatrix} \\ V_l &= \frac{1}{2}\gamma^{-1}\mathbf{s}_l^T\mathbf{s}_l + \tilde{\theta}^T\Psi^{-1}\tilde{\theta}, && (18) \end{aligned}$$

where $\tilde{X}$ and $\tilde{Y}$ are position errors (the difference between the current position and the position setpoint), $\tilde{\theta}$ is a vector containing the estimation errors of γ^{-1}, f_1, and f_2, and Ψ is an adaptive gain. Given a positive diagonal controller gain matrix K_l, it can be proved that the following control law

$$g\begin{bmatrix} \hat{z}_{d1} \\ \hat{z}_{d2} \end{bmatrix} = -K_l\mathbf{s}_l + \frac{d^2}{dt^2}\begin{bmatrix} X \\ Y \end{bmatrix} + \Upsilon\hat{\theta}, \tag{19}$$

with the term $\Upsilon\hat{\theta}$ written as

$$\Upsilon\hat{\theta} = \left[\frac{d^3}{dt^3}\begin{bmatrix} X \\ Y \end{bmatrix} - \frac{d}{dt}\mathbf{s}_l \begin{matrix} R_{11}/m & R_{12}/m \\ R_{21}/m & R_{22}/m \end{matrix}\right]\begin{bmatrix} \hat{\gamma}^{-1} \\ \hat{f}_1 \\ \hat{f}_2 \end{bmatrix}, \tag{20}$$

and the adaptive law

$$\dot{\hat{\theta}} = -\Psi\Upsilon^T\mathbf{s}_l, \tag{21}$$

make the time derivative of the proposed Lyapunov function candidate negative definite

$$\dot{V}_l = -\mathbf{s}_l^T K_l \mathbf{s}_l \leq 0. \tag{22}$$

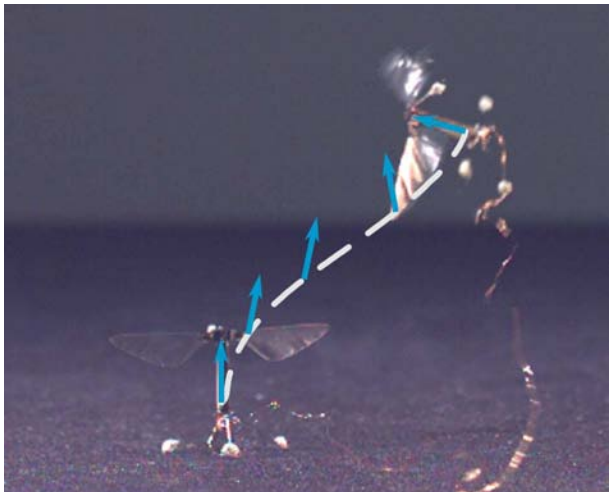

Fig. 4. A composite image of an open-loop flight overlaid by a reconstruction of the trajectory. This demonstrates that without active control, the robot crashed in 370ms.

Again, the invariant set theorem can be applied to ensure the stability of the system. In case of hovering, the position setpoint is constant. In more general cases, the controller also possesses the ability to track time-varying setpoints as the first and second derivative of the setpoint are incorporated into the composite variable $\mathbf{s}_l$.

C. Adaptive Altitude Controller

The altitude controller has a structure similar to the lateral controller in the preceding section, but with only one dimensional dynamics and a feedforward term to account for gravity. The input to the altitude dynamics is, however, the commanded thrust. The adaptive part is responsible for estimating the thrust offset and a time constant similar to γ in the lateral controller.

The main assumption on the altitude controller is that the robot orientation is always upright, thus the generated thrust is always aligned with the vertical axis. The primary reason for assumption is to preserve the limited control authority for the more critical attitude controller. To illustrate, a tilted robot may lose altitude due to a reduction in thrust along the inertial vertical axis. Instead of producing more thrust to compensate, we prioritize control authority to the attitude controller to bring the robot upright and reorient the thrust to the vertical axis.

V. Experiments

A. Experimental Setup

Flight control experiments are performed in a flight arena equipped with eight motion capture *VICON* cameras, providing a tracking volume of $0.3 \times 0.3 \times 0.3$m. The system provides position and orientation feedback by tracking the position of four retroreflective markers at a rate of 500Hz. Orientation feedback is given in the form of Euler angles that can immediately be converted into a rotation matrix.

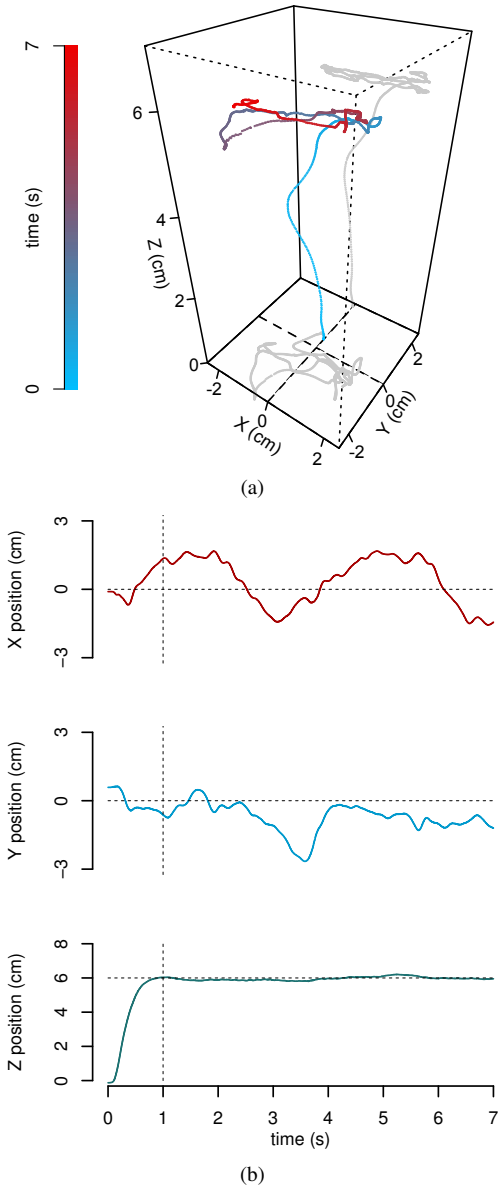

Fig. 5. Trajectory plots of a 7-second hovering flight. (a) A three-dimensional reconstruction of the trajectory. Line color is associated with time as indicated in the left bar graph. (b) Plots of positions in the inertial frame. The horizontal dashed lines indicate the setpoint positions and the vertical dashed lines indicate when the adaptive part weres fully activated. It can be seen that the vehicle generally stayed within 2cm of the setpoint.

Computation for control is carried out on external computers using an xPC Target system (*Mathworks*), which operates at 10kHz for both input sampling and output signal generation. Power is delivered to the robot via a 0.6m long bundle of four 51-gauge copper wires. The latency of the complete experimental setup was found to be approximately 12 ms–less than two wing beats.

The lack of direct velocity and angular velocity measurement requires us to estimate both velocities via the use of filtered derivatives. The approach allows some attenuation of high frequency disturbances, but the estimates suffer from delays introduced by filter phase shifts. With a reliable

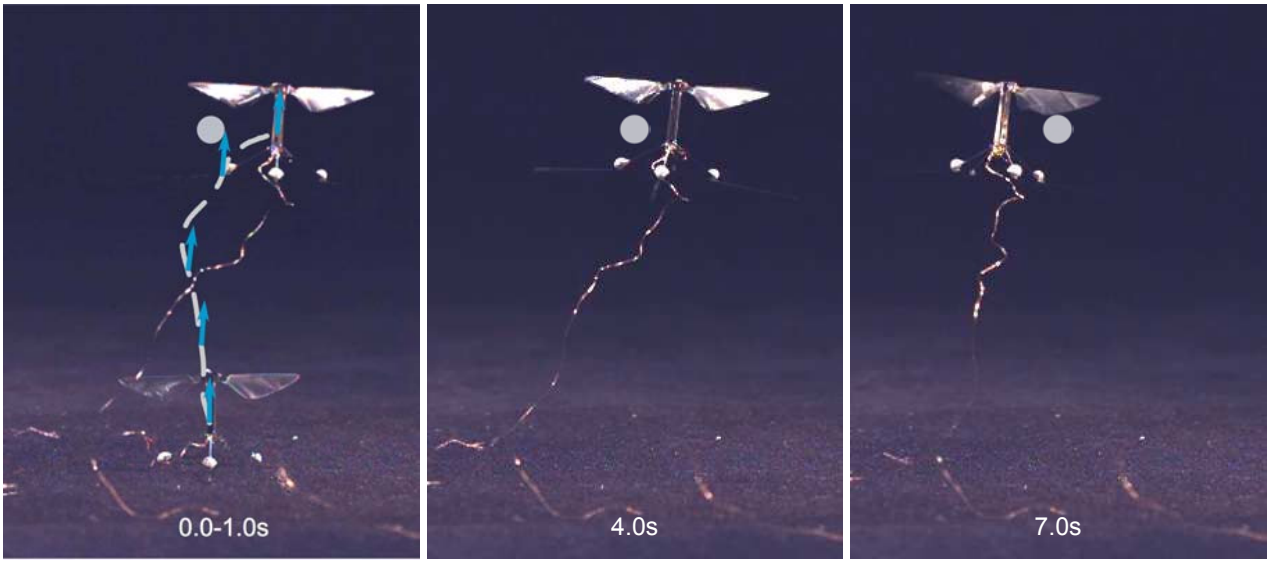

Fig. 6. Frames from a video footage taken by a high-speed camera at 240 frames per second demonstrating a hovering flight. The white dot indicates the setpoint. The left composite image is overlaid by a reconstructed takeoff trajectory from $0.0 - 1.0$s. The middle and the right images are from 4.0s and 7.0s respectively.

dynamical model, this could be alleviated by the use of observers. In this work, however, this delay is present and not considered by the controller.

B. Open-loop trimming

Initially, the vehicle is mounted on a static setup and a high-speed video camera is used to measure the flapping amplitude of the robot at various frequencies to determine the resonant frequency of the system and to characterize the suitable operating point where asymmetry between the two wings is minimized. Once the operating frequency is chosen, trimming flights are executed in the flight arena.

Open-loop trimming is carried out by commanding the robot to produce constant thrust and torques. Visual feedback and state feedback are used to determine the amount of undesired bias torques. The process is repeated with a new set of offset torques in an attempt to minimize the observed bias torque. Due to the inherent instability of the robot, a successful open-loop flight usually crashes in less than 0.5s. This emphasizes the need of active control for the vehicle. An automatic switch-off routine is also implemented to cut off the power when the robot deviates more than 60° from vertical to prevent damages from crashing. An example of a well-trimmed open-loop flight, where the robot ascended to more than 4cm in altitude before crashing, is displayed in Fig. 4.

C. Hovering flight

Configurations obtained from open-loop flights serve as initial estimates of torque bias for closed-loop hovering flights. At the beginning, only the attitude controller and the altitude controller are active. The robot usually takes less than one second to reach the altitude setpoint. The lateral controller is initiated 0.2s into the flight, however, it is not fully activated until $t = 0.4$s. Similarly, the adaptive parts are activated 0.8s into the flight, but are not in full operation until 1.0s.

Oftentimes, the parameter estimates derived from open-loop trimming flights are sufficiently accurate for the robot to stay aloft for a few seconds while the adaptive parts enhance the performance of the controller by adjusting these estimates. Nevertheless, parameter estimates learned at the end of each flight are incorporated into the controller as new estimates. These include the torque offset (τ_o) in the attitude controller, orientation misalignment in the lateral controller (f_1, f_2), and the thrust offset in the altitude controller.

In the absence of mechanical fatigue, after a few 5-second tuning flights, estimated parameters tend to converge to constant values. At this point, the robot is typically able to maintain its altitude setpoint within a few millimeters , while the lateral precision is on the order of one to two centimeters. It is likely that local air currents or tension from the power wires is the cause of disturbances.

Fig. 5. demonstrates an example of a typical hovering flight after parameter convergence. In this circumstance, the flight lasts seven seconds, after which the power is cut off. In this sequence, the robot maintained the altitude at 6.0cm above the ground while it translated laterally around the setpoint. Still frames from a video footage of the same flight are also shown in Fig 6. More examples of hovering flights can also be found in the supplemental video.

D. Landing

In order to move away from violent crashes and simultaneously demonstrate precise maneuvers, here we show the first controlled takeoff and landing of a robotic insect. At a time of landing, the translational and angular velocities must

Fig. 7. Photograph of the robotic insect with extended landing gears. The extensions are attached to the current structure through a viscoelastic urethane material.

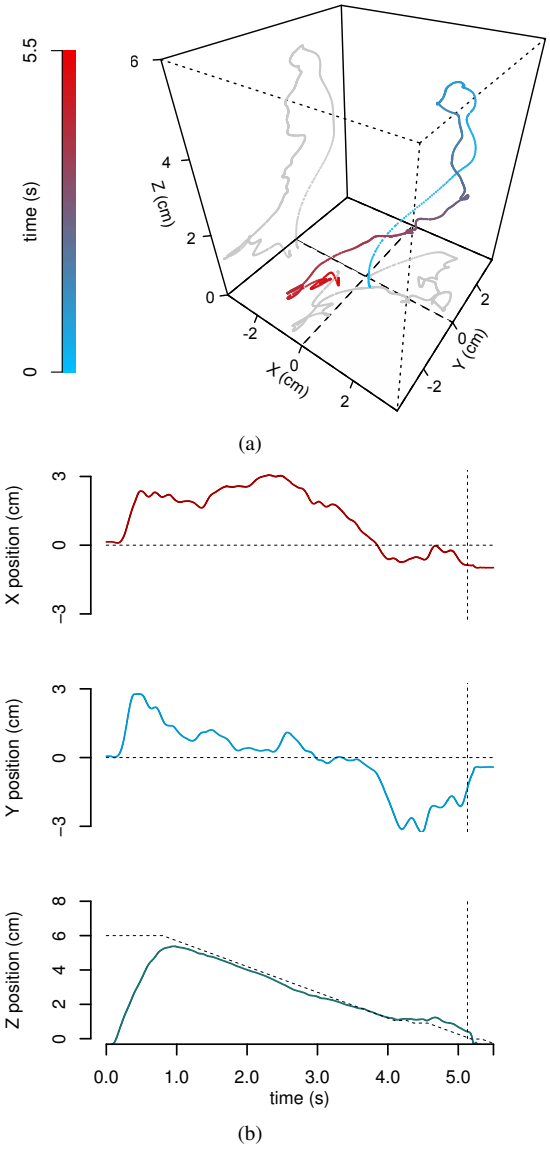

Fig. 8. Trajectory plots of a vertical takeoff and landing flight. (a) A three-dimensional reconstruction of the trajectory. Line color is associated with time as indicated in the left bar graph. (b) Plots of positions in the inertial frame. The horizontal and inclined dashed lines indicate the setpoint positions and the vertical dashed lines indicate when the adaptive parts were fully activated. The landing process started just before 1s and completed after 5s.

TABLE I

COMPARISON OF THE RMS POSITION ERRORS FROM THE NON-ADAPTIVE CONTROLLER AND THE PROPOSED ADAPTIVE CONTROLLER.

Controller	RMS errors (cm)			
	X	Y	Z	Average
Non-adaptive [1]				
Flight 1	0.76	2.35	1.59	1.67
Flight 2	1.31	1.74	1.44	1.45
Flight 3	1.50	3.15	0.90	2.06
Adaptive				
Flight 1	0.93	1.12	0.14	0.82
Flight 2	0.34	1.66	0.05	0.97
Flight 3	0.83	0.59	0.12	0.54

be relatively small, otherwise the momentum would cause the robot to crash. Moreover, when the robot approaches the ground, downwash from the flapping wings may introduce disturbances in the form of ground effects as seen in larger flying vehicles, and destabilize the robot. Here, we illustrate successful landing flights via the use of simple control strategy with the aid of mechanical landing gear.

The landing gear is designed with two goals: to widen the base of the robot and to absorb the impact of landing. Carbon fiber extensions are attached to the existing structure through a viscoelastic urethane spacer (Sorbothane). A photograph of a robot with the additional landing gear is shown in Fig. 7.

Landing is achieved by slowly reducing the altitude setpoint. To ensure that the robot remains in the nominal upright orientation and stays close to the lateral setpoint, the change in altitude setpoint is suspended when the vehicle is in an unstable state, defined as the l_2-norm of the composite variable $\mathbf{s}_a$ or $\mathbf{s}_l$ being larger than the chosen thresholds. Once the robot is less than a certain height (≈ 8mm) above the ground, the driving signals are ramped down, leaving the landing gear to absorb the impact from falling.

An example trajectory of a successful vertical takeoff and landing flight of the robotic insect is displayed in Fig. 8. In this case, the robot took off towards the altitude setpoint at 6cm and started the landing process just before 1.0s. The nominal landing speed was set at $1.5\text{cm}\cdot\text{s}^{-1}$. According to the plot, the robot followed the trajectory setpoint closely. Nevertheless, just after $t = 4$s, it can be seen that the landing was briefly suspended as the vehicle drifted away from the lateral setpoint beyond the tolerance. Eventually, the robot reached the pre-defined landing altitude and the power was ramped down after five seconds. Video footage of a few landing flights can also be found in the supplemental video.

VI. DISCUSSION AND FUTURE WORK

We have presented a comprehensive flight controller designed for a bio-inspired flapping-wing microrobot. Driven by modeling uncertainty and the nonlinear nature of the system, Lyapunov's direct method was employed to guarantee the stability of the proposed adaptive controllers. Successful hovering flights as well as vertical takeoff and landing flights were demonstrated.

Comparing with the non-adaptive controller in previous work [1], flights obtained from the proposed adaptive controller have markedly smaller position errors. Table I lists the *Root Mean Square* (RMS) errors of the measured position from the setpoint for several hovering flights performed by both controllers. Note that the average RMS errors indicate the RMS of the Euclidean distance from the setpoint. As seen in the table, the proposed controller reduces the RMS errors by approximately 50%. The improvement is most pronounced along the $\hat{Z}$ direction, thanks to the adaptive altitude controller.

Though the adaptive parts of the controller were capable of producing better parameter estimates and enhanced the flight performance, there are still avenues of possible improvements. The development of a multi-axis torque sensor would likely provide an accurate transfer function of the torque outputs. The study of flight dynamics and identification techniques may yield better models that take into account the aerodynamic damping [11], [12], which can then be incorporated into the controller design process.

Eventually, better knowledge of the system should allow flight maneuvers that depart significantly from hovering. Aggressive maneuvers as seen in quadrotors [13], nevertheless, would still be limited by the tether wire. Thus, beyond the control aspects, future work entails the integration of onboard power, sensing and computation [14]. Ultralightweight power electronics for high-voltage piezoelectric bimorphs have already been in development [15], whereas sensors such as gyroscopes, accelerometers, ocelli, and cameras for optical flow will need to be custom-built or modified to meet the limited mass and power budgets [16].

REFERENCES

[1] K. Y. Ma, P. Chirarattananon, S. B. Fuller, and R. J. Wood, "Controlled flight of a biologically inspired, insect-scale robot," *Science*, vol. 340, no. 6132, pp. 603–607, 2013.

[2] R. Wood, E. Steltz, and R. Fearing, "Optimal energy density piezoelectric bending actuators," *Sensors and Actuators A: Physical*, vol. 119, no. 2, pp. 476–488, 2005.

[3] J. Whitney, P. Sreetharan, K. Ma, and R. Wood, "Pop-up book MEMS," *Journal of Micromechanics and Microengineering*, vol. 21, no. 11, p. 115021, 2011.

[4] K. Y. Ma, S. M. Felton, and R. J. Wood, "Design, fabrication, and modeling of the split actuator microrobotic bee," in *Intelligent Robots and Systems (IROS), 2012 IEEE/RSJ International Conference on*. IEEE, 2012, pp. 1133–1140.

[5] B. M. Finio and R. J. Wood, "Open-loop roll, pitch and yaw torques for a robotic bee," in *Intelligent Robots and Systems (IROS), 2012 IEEE/RSJ International Conference on*. IEEE, 2012, pp. 113–119.

[6] C. T. Orlowski and A. R. Girard, "Dynamics, stability, and control analyses of flapping wing micro-air vehicles," *Progress in Aerospace Sciences*, 2012.

[7] J. Whitney and R. Wood, "Aeromechanics of passive rotation in flapping flight," *Journal of Fluid Mechanics*, vol. 660, no. 1, pp. 197–220, 2010.

[8] B. M. Finio, N. O. Pérez-Arancibia, and R. J. Wood, "System identification and linear time-invariant modeling of an insect-sized flapping-wing micro air vehicle," in *Intelligent Robots and Systems (IROS), 2011 IEEE/RSJ International Conference on*. IEEE, 2011, pp. 1107–1114.

[9] B. M. Finio, K. C. Galloway, and R. J. Wood, "An ultra-high precision, high bandwidth torque sensor for microrobotics applications," in *Intelligent Robots and Systems (IROS), 2011 IEEE/RSJ International Conference on*. IEEE, 2011, pp. 31–38.

[10] J.-J. E. Slotine, W. Li *et al.*, *Applied nonlinear control*. Prentice-Hall Englewood Cliffs, NJ, 1991, vol. 199, no. 1.

[11] P. Chirarattananon and R. J. Wood, "Identification of flight aerodynamics for flapping-wing microrobots," in *Robotics and Automation (ICRA), 2013 IEEE International Conference on*. IEEE, 2013, to appear.

[12] V. Klein and E. A. Morelli, *Aircraft system identification: theory and practice*. American Institute of Aeronautics and Astronautics Reston, VA, USA, 2006.

[13] D. Mellinger, N. Michael, and V. Kumar, "Trajectory generation and control for precise aggressive maneuvers with quadrotors," *The International Journal of Robotics Research*, vol. 31, no. 5, pp. 664–674, 2012.

[14] R. Wood, B. Finio, M. Karpelson, K. Ma, N. Pérez-Arancibia, P. Sreetharan, H. Tanaka, and J. Whitney, "Progress on 'pico' air vehicles," *The International Journal of Robotics Research*, vol. 31, no. 11, pp. 1292–1302, 2012.

[15] M. Karpelson, G.-Y. Wei, and R. J. Wood, "Driving high voltage piezoelectric actuators in microrobotic applications," *Sensors and Actuators A: Physical*, 2012.

[16] W.-C. Wu, L. Schenato, R. J. Wood, and R. S. Fearing, "Biomimetic sensor suite for flight control of a micromechanical flying insect: design and experimental results," in *Robotics and Automation, 2003. Proceedings. ICRA'03. IEEE International Conference on*, vol. 1. IEEE, 2003, pp. 1146–1151.